optica

Dynamic bound states in the continuum

Kebin Fan,[1] Ilya V. Shadrivov,[2] and Willie J. Padilla[1,*]

[1]Department of Electrical and Computer Engineering, Duke University, Durham, North Carolina 27708, USA
[2]Nonlinear Physics Centre, Research School of Physics and Engineering, Australian National University, Canberra, ACT 2601, Australia
*Corresponding author: willie.padilla@duke.edu

Received 10 August 2018; revised 4 January 2019; accepted 4 January 2019 (Doc. ID 341933); published 8 February 2019

All-dielectric metasurfaces are a versatile platform to investigate a host of unconventional physical scattering responses. Effects, including high absorption and Huygens' surfaces, have been demonstrated; however, a more exotic materialization—termed bound states in the continuum (BSCs)—exists and consists of nonradiating localized waves that lie within the energy spectrum of the continuum. Here we experimentally demonstrate a dynamic BSC at terahertz frequencies that realizes a material-limited high-quality factor (Q) resonance $Q = 8.7 \times 10^3$, which may be modified by over 2 orders of magnitude through photodoping with band gap light. We elucidate the nature of the BSC resonance, and our experimental results are well supported by eigenvalue and S-parameter simulations. The demonstrated system and underlying theory establish a path to realize extremely high-Q dynamic resonances, which may be useful for detection of hazardous materials and frequency-diverse imaging.

https://doi.org/10.1364/OPTICA.6.000169

The ability to confine and localize electromagnetic waves is a powerful concept that has long been a goal of numerous theoretical and experimental investigations. One particularly intriguing approach to achieve light localization is by exploiting the so-called bound states in the continuum (BSCs) [1,2]. The concept of BSCs originated in quantum mechanics and can be described as discrete solutions of the single-particle Schrödinger equation embedded in the continuum of positive-energy states [3]. Such bound states exist in the continuum, but possess infinite lifetime, i.e., an infinite quality factor, ($Q = \infty$), and thus are perfectly localized with no coupling to the vacuum. However, in an open system, the effective Hamiltonian of Maxwell's equations can be described as a non-Hermitian matrix, which includes discrete bound states of the scatters, and the coupling between the bound and scattering states. Therefore, the associated eigenfrequencies are complex $\omega = \omega_0 - i\gamma$, where ω_0 represents the resonant frequency and—for a lossless system—γ is the damping rate of radiation to free space, i.e., lifetime of the resonance.

There are several physical conditions that may lead to BSCs, and they may be characterized by the mechanism responsible for electromagnetic wave localization [4–6]: (i) symmetry protected [7–9], (ii) Fabry–Perot [10], (iii) resonance interference [2,11–14], and (iv) accidental zero [15]. More specifically, the system we investigate supports various Bloch BSCs, and here we confine our study to a particularly intriguing symmetry protected BSC with zero Bloch vector, which arises due to violation of the uniqueness theorem [9,16–20]. The Bloch BSC is characterized by the intersection of three zeros in (ω, k) space, i.e., those of the reflectivity coefficient (r), transmissivity coefficient (t), and the tangential wavevector ($k_\parallel$), and we denote this state by (ω_B, k_B).

Our dynamic BSC is realized in a two-dimensional silicon-based metasurface operating at terahertz (THz) frequencies which—as we will demonstrate—can be tuned through optical photodoping. The metasurface consists of free-standing low-loss cylindrical resonators and realizes several high-quality factor (Q) modes near 1 THz. The silicon carrier density is modified through photodoping, thereby achieving control of the Q factor of the BSC. In Fig. 1(a), we show a schematic depicting optical control of the BSC and a SEM image of the fabricated structure is shown in Fig. 1(b). The BSC is freely suspended and supported with thin interconnects between unit cells. The use of high-resistivity silicon—coupled with the lack of a substrate—allows for an extremely low material (nonradiative) loss rate. Thus, the BSC mode within the all-dielectric metasurface presented in Fig. 1 can be precisely controlled by its radiative and nonradiative damping rates (γ and δ, respectively) through modification of the symmetry of the system with respect to the k vector ($\mathbf{k}$) of incident light, and/or through photodoping. The surface normal $\hat{\mathbf{n}}$ lies along the cylindrical axis (oriented in the $\hat{\mathbf{z}}$ direction), and we define the incident angle θ as $\hat{\mathbf{k}} \cdot \hat{\mathbf{n}} = \cos\theta$, where the usual definition applies, $\mathbf{k} = |k|\hat{\mathbf{k}}$. Our study focuses on results for the transmission only in transverse magnetic (TM) polarization.

The unique state of the BSC is highlighted in Fig. 1(c), which shows results taken from S-parameter simulations, consisting of $t(\omega)$ (red colors) and $r(\omega)$ (blue colors) as a function of θ. In Fig. 1(d), the dispersion diagram ω vs $k_{||}$ is calculated from Fig. 1(c) as $k_{||}(\frac{2\pi}{a}) = \frac{\omega}{c}\sin\theta$, and we plot only the extrema of r and t. The solid red and blue curves are $t = 0$ and $r = 0$, respectively. The principle of the BSC is that incident light of frequency and k vector (ω_B, k_B) cannot couple to the symmetry-protected BSC, since it is perfectly localized. However,

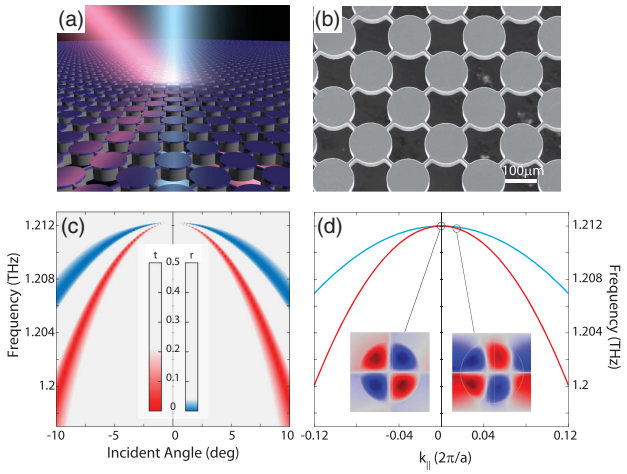

Fig. 1. (a) Illustration of all-dielectric metasurfaces showing optical photodoping of the structure. (b) SEM image of the fabricated free-standing silicon structure with a diameter of 132 μm, height of 50 μm, and a periodicity of 168 μm. The scale bar is 100 μm. (c) Simulated angular dependence of the transmission and reflection. Red colors denote $t \approx 0$ and blue colors $r \approx 0$. (d) dispersion diagram $(\omega, k_{||})$ showing $t = 0$ (red curve) and $r = 0$ (blue curve). Left inset shows Ez for the symmetry-protected BSC, and right inset shows Ez for the broken symmetry state.

if $\omega \neq \omega_B$ or $k \neq k_B$, then the symmetry is broken, and incident light may couple with the BSC. The electromagnetic signature of this coupling is a high-Q mode characterized by rapid variation of t and r as a function of ω or k [18–20].

In Fig. 2, we show S-parameter simulations of the free-standing silicon metasurface as a function of frequency. The red curve in Fig. 2(a) shows $t(\omega)$ for normal incidence, and we find that, at low frequencies $t(\omega)$, it is relatively high before undergoing an absorptive resonance (minimum) near 0.96 THz —we designate this mode (e1), since it is the first (lowest energy) even eigenmode. Continuing to higher frequencies, another absorptive minimum occurs at approximately 1.09 THz, and we find that this eigenmode possesses odd character (o1). Figure 2 (b) shows $t(\omega)$ for $\theta = 10°$, and we find—in addition to the occurrence of modes present in the normally incident case—two

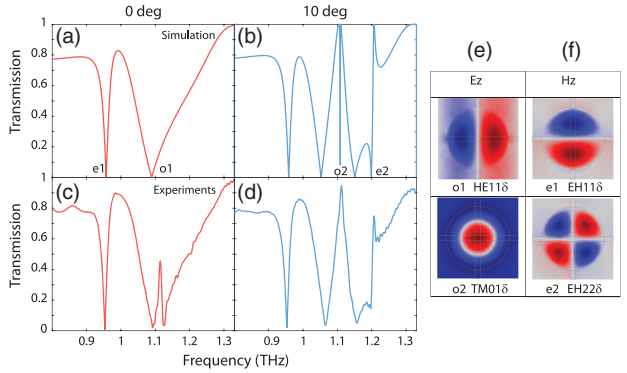

Fig. 2. Simulated transmission coefficients of the BSC metasurface for (a) normal and (b) 10° angle of incidence. (c) and (d) are the corresponding experimentally measured results. (e) Normalized z component of electric field for odd eigenmodes at the mirror symmetric xy plane of the cylinders. (f) Normalized z component of magnetic field for even eigenmodes at the mirror symmetric xy plane of the cylinders.

other modes with one even (e2) and one odd (o2) mode. It is important to note that all the new modes resulting from oblique incidence possess extremely narrow linewidth, thus indicating high-Q factors. Figures 2(e) and 2(f) show the normalized z component of electric and magnetic fields in the σ_{xy} mirror plane for odd and even modes, respectively. In what follows, we will focus on the even eigenmode (e2), which lies at a frequency of 1.2 THz, and has been shown to be a BSC with zero Bloch wave vector [4]. We thus have a system consisting of an even eigenmode (e2) embedded within a continuum of odd symmetry (o1).

The BSC was characterized using THz time-domain spectroscopy. In Fig. 2, we show the experimental $t(\omega)$ for $\theta = 0°$ (c), and we find a good match to simulation, observing both (e1) and (o1) modes. We note that our THz spectroscopic system uses lenses with an $f/\# = 4$, and thus we also find signature of (e2) at $\theta = 0°$. At oblique incidence $\theta = 10°$ [Fig. 1(d)] we find a high-Q mode at 1.2 THz, i.e., (e2), and it is strongly enhanced compared to normal incidence, spanning from a minimum of about $t = 14\%$ to a maximum of 75%, i.e., a $\Delta t = 61\%$.

In Fig. 3(b), we show the dispersion relation of the metasurface for $k_{||}$ determined with eigenvalue simulations. The simulated transmission coefficients for normal incidence (gray curve) and $\theta = 1.5°$ (blue curve) are shown in Fig. 3(a) for comparison. The high-Q e2 mode only exists for off-normal $t(\omega)$ and occurs near 1.2 THz. The red curve from the eigenvalue simulation shown in Fig. 3(b) lies close to the light line (dashed black curve) for low frequencies, before undergoing band folding at the Brillouin zone boundary, and intersecting the gamma point at a frequency of approximately 1.2 THz.

Eigenvalue simulations were undertaken in order to determine radiative and nonradiative properties of the Bloch BSC. A complex mode frequency $\tilde{\omega} = \omega_1 - i\omega_2$ results, where ω_1 is the resonant frequency of the mode and ω_2 is the damping rate. Two terms contribute to the imaginary term $\omega_2 = \gamma + \delta$, where, as mentioned previously, γ is damping of the mode due to radiation, and δ is damping due to material loss. Eigenvalue simulations may

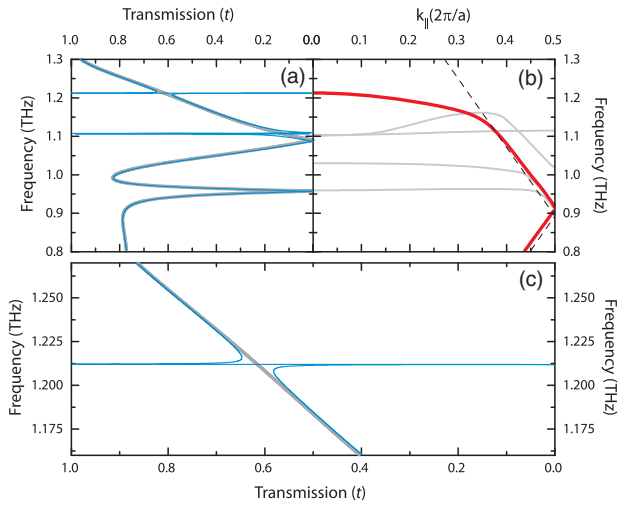

Fig. 3. Frequency-dependent transmission coefficient (a) and (c), simulated at normal incidence (gray curve) and $\theta = 1.5°$ (blue curve) for lossless cylinders. (b) Eigenvalue simulation of the dispersion diagram for TM polarization. The black dashed line is the light line. The periodicity is $a = 168$ μm. (c) Zoomed-in region of the transmission coefficient near ω_B shown in (a).

be performed with and without material loss, and thus one may determine the separate γ and δ contributions to ω_2. Results from eigenvalue simulation are presented in Fig. 4(a), where we plot the Q factor (red curve left axis) and radiative loss rate γ (blue curve right axis), determined from eigenvalue simulation for e2 as a function of incident angle. As can be observed, $\gamma = 0$ at $\theta = 0°$, and thus the even e2 mode is unable to couple to free-space radiation at normal incidence. However, as θ is increased, the Q factor reduces while the damping rate increases, and the high-Q BSC mode e2 may radiate and thus couple to incident THz radiation. The inset to Fig. 4(a) shows γ (blue curve) and δ (gold curve) for $0 \le \theta \le 2°$. Our silicon has a resistivity $\rho \ge 1000\ \Omega$ cm, corresponding to a carrier density of 1.4×10^{13} cm^{-3} for p-type silicon. We thus have an expected angle-independent material loss rate of $\delta = 0.436$ ns^{-1}. At near-normal angles of incidence, the radiative loss rate is approximately zero, and the material loss rate corresponds to a Q factor of $Q = 8733$.

In Fig. 4(b), the left axis plots the Q factor (open black symbols), and the right axis plots the radiative (blue curve) and material loss (gold curve) rates, all as a function of doping for an incident angle of $\theta = 10°$. The dashed vertical gray line shows the doping value where $\gamma = \delta$. The real ($\Delta\omega_r = \mathrm{Re}\{\omega_e - \omega_B\}/\mathrm{Re}\{\omega_B\}$) and imaginary ($\Delta\omega_i = \mathrm{Im}\{\omega_e - \omega_B\}/\mathrm{Im}\{\omega_B\}$)) relative frequency difference are plotted on the left and right vertical axes of Fig. 4(c), respectively, and are obtained from eigenvalue simulations for the lossy metasurface at normal incidence. Here $\omega_e(n_d)$ is the doping-dependent complex eigenfrequency and $\omega_B = 1.2133 + i6.9461 \times 10^{-5} \times 2\pi$ THz for high-resistive silicon. Remarkably, we find that for modest photodoping values of $n_d = 1.9 \times 10^{15}/\mathrm{cm}^3$, $\Delta\omega_r$ only changes by approximately 1%, whereas $\Delta\omega_i$ changes by nearly a factor of 300, corresponding to a change in the Q factor by 2 orders of magnitude.

Having characterized the transmissive properties of the all-dielectric BSC metasurface, we demonstrate dynamical behavior of the e2 eigenmode using optical excitation. The metasurface is kept at an incident angle of $\theta = 10°$, and we use an optical pump to produce carriers in the silicon metasurface. The optical source consists of a multimode laser diode with a wavelength of 980 nm. In Fig. 5(a), we show the experimental transmission coefficient as a function of frequency at $\theta = 10°$, for a number of optical pump powers ranging from undoped (black curve) to 536 mW (red curve), which correspond to photodoped carrier density of $1.03 \times 10^{16}/\mathrm{cm}^3$. As can be observed, with no photon power, the e2 mode realizes a relatively large response—characterized by the difference between the high (t_{high}) and low (t_{low}) transmission values $\Delta t \equiv t_{\mathrm{high}} - t_{\mathrm{low}} = 61\%$. However, as pump power is increased, the strength of the e2 mode is monotonically reduced, as shown in the inset to Fig. 5, which shows Δt as a function of pump power. In Fig. 5(b), we show the simulated $t(\omega)$ for a number of different doping carrier densities.

We next turn toward discussion of the results. The S-parameter and eigenvalue simulations presented in Figs. 1(c) and 1(d) verify that as the $t = 0$ and $r = 0$ curves approach $\theta = 0$, they both converge to the same point, i.e., (ω_B, k_B). Thus, although normally incident light achieves $t = 65\%$ at $\omega = \omega_B$, it is unable to couple to the e2 BSC mode, since it possesses $t = 0$, $r = 0$, and $k_{||} = 0$, i.e., it is symmetry-protected—see gray curve in Fig. 3(a) and the red curve of Fig. 3(b) [7,21]. However, once the symmetry is broken through use of off-normal light, $k_{||}$ moves

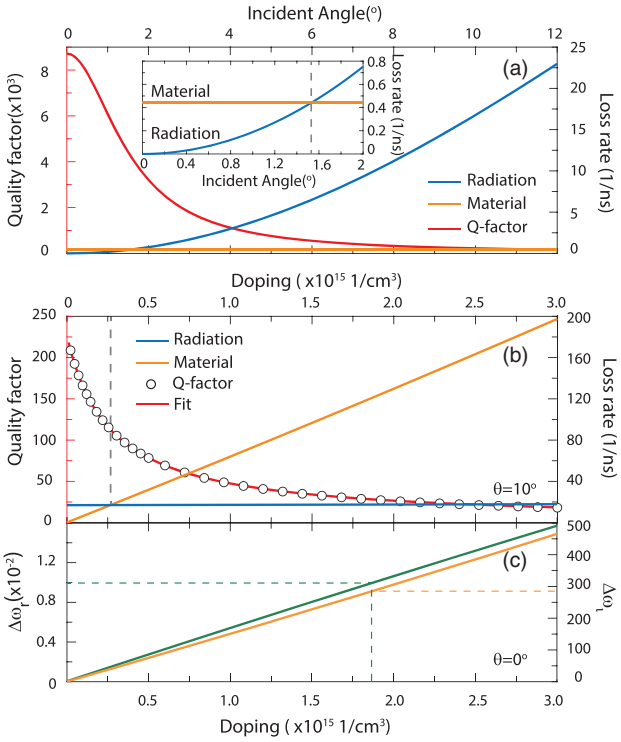

Fig. 4. Simulation of the quality factor (red left axis), radiative (blue), and nonradiative (gold) loss rates (right axis) as a function of (a) incident angle and (b) doping. Inset to (a) shows a zoomed-in region for angles up to 2°. Incident angle in (b) is $\theta = 10°$. (c) Dependence of the real (green) and imaginary (gold) parts of the relative change in complex eigenfrequency, defined in the text. Green and gold dashed curves in (c) identify doping values needed for 1% change in $\Delta\omega_r$ and a factor of 300 change in $\Delta\omega_i$, respectively.

away from k_B, and the frequency locations of $t = 0$ and $r = 0$ deviate from each other, thus permitting coupling to the high-Q BSC [22]. Indeed, the radiative rate shown in Fig. 4(a) is zero at normal incidence $\gamma(\theta = 0) = 0$, thus suggesting $Q = \infty$ in the limit of zero material loss. However, at oblique incidence, the occurrence of radiative loss reduces the Q factor, where its value is inversely proportional to the difference in frequency between the $r = 0$ and $t = 0$ curves.

Notably, we find that the $r = 0$ and $t = 0$ curves of the dispersion relation [Fig. 1(d)] all realize a specific $k_{||}$ dependence. Fits to the $r = 0$ and $t = 0$ curves in Fig. 1(d) find

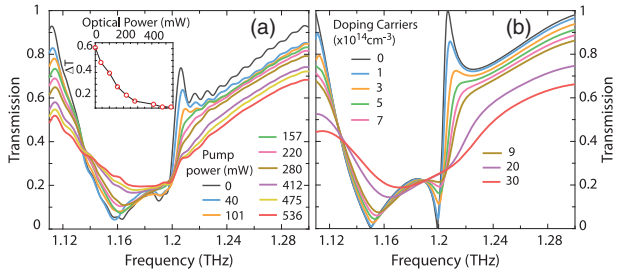

Fig. 5. (a) Experimental and (b) simulated off-normal ($\theta = 10°$) transmission coefficient as a function of frequency for different optical pump fluence. The black curve shows the transmission without photoexcitation on the silicon metasurface. Inset to (a) shows the $\Delta t \equiv t_{\mathrm{max}} - t_{\mathrm{min}}$ as a function of optical pump power in the vicinity of the BSC.

$\omega = -0.3248k_{||}^{1.964} + 1.212 \times 2\pi$ THz, and $\omega = -0.7045k_{||}^{1.924} + 1.212 \times 2\pi$ THz, respectively, i.e., both are approximately quadratic and have the same vertical axis intercept of $\omega_B = 1.212 \times 2\pi$ THz. The character of the Bloch BSC shown in Fig. 2(b) is such that, as a function of increasing frequency, it first undergoes a minimum t, before achieving a maximum. This particular form is well characterized as a Fano resonance, where the asymmetry is due to interference between a resonant mode (e2) and a broad continuum—in this case (o1) [14]. Thus the form of the Fano asymmetry may be modified by moving the frequency location of the Bloch BSC (i.e., changing the periodicity) to a region where the transmitted phase is different, thereby yielding an alternative interference condition.

In our case, the Bloch BSC arises from a leaky mode, which becomes confined to the metasurface in the $k_{||}$ direction due to band folding at the Brillouin zone boundary, as shown in Fig. 3. Similar modes in photonic crystals have been observed, and are termed guided modes when they occur below the light line, and guided resonances above [23,24]. Although a true BSC achieves an infinite Q factor, the system realized is finite in spatial extent and exhibits nonradiative loss, which ultimately limits the Q. An ideal BSC with a $Q = \infty$ resonance requires an infinitely extended system in order to cancel radiative losses. That is, the leaky mode supported by the infinitely extended array experiences destructive interference leading to a cancellation of radiative losses. The mode is thus effectively bounded to the array with no radiation. In any real system (with small material loss), the array is finite, and thus the Q may be large, but not infinite. However, in a finite system, the number of resonators (N) sets the Q value—the exact dependence for a symmetry-protected BSC is $Q \propto N^2$ [9]. Thus, since the Q factor scales quadratically with the number of resonators, one effective route to achieve higher-Q BSCs is to make the size of the periodic array larger.

We find our BSC may achieve a material-limited Q factor of $Q = 8733$, at incidence angles infinitesimally close to $\theta = 0°$, as shown in Fig. 4(a). However, as the incident angle increases, the radiative losses (blue curve) increase until they achieve a value equal to the material loss (gold curve), and dominate for $\theta \geq 1.5°$. On the other hand, as observed in Fig. 4(b), we find that γ is largely independent of photodoping fluence, but that the material loss rate realizes an approximate linear dependence. Thus, as shown in Fig. 4(b), the effect of photodoping is to increase the material loss, thereby reducing the Q factor (red curve) and diminishing the strength of the BSC. It is important to detail that although the radiative loss is doping independent—as can be observed from the blue curve in Fig. 4(b)—it is nonzero. Thus, the total Q factor (Q_T) of the BSC mode consists of two contributions—that of the material loss Q_δ, and the radiative loss Q_γ—which add in parallel [14]. At an incident angle of 10°, $Q_\gamma^{-1} = 0.00442$, which leads to a maximum value of the total Q factor at low doping values. The solid red curve in Fig. 4(b) is a fit of the total Q factor $Q_T^{-1} = Q_\delta^{-1} + Q_\gamma^{-1}$, where $Q_\delta^{-1} = \alpha n_d$, with n_d the carrier density resulting from photodoping the silicon metasurface, and $\alpha = 1.68 \times 10^{-17}$ cm^3. As can be observed, the fit matches the simulated total Q factor [open black symbols in Fig. 4(b)] well, thus confirming the theory and the expected dependence of the BSC Q factor on photodoping.

Simulations presented in Fig. 4(c) are for $\theta = 0$ and further elucidate the mechanism responsible for the dynamic Q factor and its dependence on photodoping. The resonance frequency of the Bloch BSC does not change significantly for doping values explored, as demonstrated by $\Delta\omega_r$ shown in Fig. 4(c). However, $\Delta\omega_i$ changes by a factor of 300, where $\Delta\omega_r$ only changes by 0.01 for doping values of approximately 1.9×10^{15}/cm^3 [shown in Fig. 4(c)], corresponding to a photodoping power of 100 mW at a wavelength of 980 nm. These results indicate that the reduction of the BSC Q factor is not a result of shifting away from (ω_B, k_B), but rather from the significant increase in the material loss rate [9].

We have proposed and experimentally demonstrated dynamic control of a BSC in a silicon metasurface. Off-normal incident light permits coupling to the high-Q BSC, which may then be controlled in real time with band gap light. Eigenvalue simulations indicate a maximum achievable Q factor of $Q = 8.7 \times 10^3$ in this system. The mechanism underlying control of the BSC is through modification of the complex eigenfrequency via photodoping—or equivalently the complex refractive index $\tilde{n} = n_1 + in_2$—which serves to increase the loss (n_2), thereby increasing the nonradiative loss rate and reducing the Q. Although we have chosen to relax the symmetry by introducing off-normal incident light, similar response is expected at normal incidence if instead the BSCs rotational symmetry is broken. Our demonstration of dynamic control of BSCs can be leveraged for applications requiring narrow bandwidth and spatial filtering, leading to more compact, efficient, and versatile photonic components [25–29].

Funding. U.S. Department of Energy (DOE) (DE-SC0014372); Australian Research Council (ARC); National Science Foundation (NSF) (ECCS-1542015); National Nanotechnology Coordinated Infrastructure (NNCI).

Acknowledgment. KF and WJP acknowledge support from the DOE. IVS acknowledges support from the Australian Research Council through the Future Fellowship Scheme.

See Supplement 1 for supporting content.

REFERENCES

1. F. H. Stillinger and D. R. Herrick, "Bound states in the continuum," Phys. Rev. A **11**, 446–454 (1975).
2. H. Friedrich and D. Wintgen, "Interfering resonances and bound states in the continuum," Phys. Rev. A **32**, 3231–3242 (1985).
3. J. von Neumann and E. P. Wigner, in *Über merkwürdige diskrete Eigenwerte* (Springer Berlin Heidelberg, 1993), pp. 291–293.
4. E. N. Bulgakov and A. F. Sadreev, "Bloch bound states in the radiation continuum in a periodic array of dielectric rods," Phys. Rev. A **90**, 053801 (2014).
5. E. N. Bulgakov and A. F. Sadreev, "Light trapping above the light cone in a one-dimensional array of dielectric spheres," Phys. Rev. A **92**, 023816 (2015).
6. C. W. Hsu, B. Zhen, A. D. Stone, J. D. Joannopoulos, and M. Soljačić, "Bound states in the continuum," Nat. Rev. Mater. **1**, 16048 (2016).
7. Y. Plotnik, O. Peleg, F. Dreisow, M. Heinrich, S. Nolte, A. Szameit, and M. Segev, "Experimental observation of optical bound states in the continuum," Phys. Rev. Lett. **107**, 183901 (2011).
8. J. Lee, B. Zhen, S.-L. Chua, W. Qiu, J. D. Joannopoulos, M. Soljačić, and O. Shapira, "Observation and differentiation of unique high-q optical resonances near zero wave vector in macroscopic photonic crystal slabs," Phys. Rev. Lett. **109**, 067401 (2012).
9. M. A. Belyakov, M. A. Balezin, Z. F. Sadrieva, P. V. Kapitanova, E. A. Nenasheva, A. F. Sadreev, and A. A. Bogdanov, "Experimental observation of symmetry protected bound state in the continuum in a chain of dielectric disks," arXiv:1806.01932 (2018).

10. D. C. Marinica, A. G. Borisov, and S. V. Shabanov, "Bound states in the continuum in photonics," Phys. Rev. Lett. **100**, 183902 (2008).
11. Y. Yang, C. Peng, Y. Liang, Z. Li, and S. Noda, "Analytical perspective for bound states in the continuum in photonic crystal slabs," Phys. Rev. Lett. **113**, 037401 (2014).
12. T. Lepetit and B. Kanté, "Controlling multipolar radiation with symmetries for electromagnetic bound states in the continuum," Phys. Rev. B **90**, 241103 (2014).
13. M. V. Rybin, K. L. Koshelev, Z. F. Sadrieva, K. B. Samusev, A. A. Bogdanov, M. F. Limonov, and Y. S. Kivshar, "High-*q* supercavity modes in subwavelength dielectric resonators," Phys. Rev. Lett. **119**, 243901 (2017).
14. A. A. Bogdanov, K. L. Koshelev, P. V. Kapitanova, M. V. Rybin, S. A. Gladyshev, Z. F. Sadrieva, K. B. Samusev, Y. S. Kivshar, and M. F. Limonov, "A direct link between Fano resonances and bound states in the continuum," arXiv:1805.09265 (2018).
15. E. Bulgakov and A. Sadreev, "Formation of bound states in the continuum for a quantum dot with variable width," Phys. Rev. B **83**, 235321 (2011).
16. L. Landau and E. Lifshitz, "Chapter 6 – electromagnetic waves," in *The Classical Theory of Fields*, L. Landau and E. Lifshitz, eds., 4th ed., Vol. **2** of Course of Theoretical Physics (Pergamon, 1975), pp. 109–129.
17. B. Anne-Sophie and S. Felipe, "Guided waves by electromagnetic gratings and non-uniqueness examples for the diffraction problem," Math. Methods Appl. Sci. **17**, 305–338 (1994).
18. S. P. Shipman and S. Venakides, "Resonant transmission near nonrobust periodic slab modes," Phys. Rev. E **71**, 026611 (2005).
19. S. P. Shipman and H. Tu, "Total resonant transmission and reflection by periodic structures," SIAM J. Appl. Math. **72**, 216–239 (2012).
20. L. Yuan and Y. Y. Lu, "Propagating bloch modes above the lightline on a periodic array of cylinders," J. Phys. B **50**, 05LT01 (2017).
21. J. M. Foley, S. M. Young, and J. D. Phillips, "Symmetry-protected mode coupling near normal incidence for narrow-band transmission filtering in a dielectric grating," Phys. Rev. B **89**, 165111 (2014).
22. E. N. Bulgakov, D. N. Maksimov, P. N. Semina, and S. A. Skorobogatov, "Propagating bound states in the continuum in dielectric gratings," J. Opt. Soc. Am. B **35**, 1218–1222 (2018).
23. M. Kanskar, P. Paddon, V. Pacradouni, R. Morin, A. Busch, J. F. Young, S. R. Johnson, J. MacKenzie, and T. Tiedje, "Observation of leaky slab modes in an air-bridged semiconductor waveguide with a two-dimensional photonic lattice," Appl. Phys. Lett. **70**, 1438 (1997).
24. S. Fan and J. D. Joannopoulos, "Analysis of guided resonances in photonic crystal slabs," Phys. Rev. B **65**, 235112 (2002).
25. A. Kodigala, T. Lepetit, Q. Gu, B. Bahari, Y. Fainman, and B. Kanté, "Lasing action from photonic bound states in continuum," Nature **541**, 196–199 (2017).
26. E. Penzo, S. Romano, Y. Wang, S. Dhuey, L. Dal Negro, V. Mocella, and S. Cabrini, "Patterning of electrically tunable light-emitting photonic structures demonstrating bound states in the continuum," J. Vac. Sci. Technol. B **35**, 06G401 (2017).
27. L. Carletti, K. Koshelev, C. De Angelis, and Y. Kivshar, "Giant nonlinear response at the nanoscale driven by bound states in the continuum," Phys. Rev. Lett. **121**, 033903 (2018).
28. W. Zhang, A. Charous, M. Nagai, D. M. Mittleman, and R. Mendis, "Extraordinary optical reflection resonances and bound states in the continuum from a periodic array of thin metal plates," Opt. Express **26**, 13195 (2018).
29. S. D. Krasikov, A. A. Bogdanov, and I. V. Iorsh, "Nonlinear bound states in the continuum of a one-dimensional photonic crystal slab," Phys. Rev. B **97**, 224309 (2018).